Available at www.sciencedirect.com

ScienceDirect

journal homepage: www.elsevier.com/locate/he

Post-test evaluation of oxygen electrodes from solid oxide electrolysis stacks☆

Jennifer R. Mawdsley[a,*], *J. David Carter*[a], *A. Jeremy Kropf*[a], *Bilge Yildiz*[b], *Victor A. Maroni*[a]

[a]*Chemical Sciences and Engineering Division, Argonne National Laboratory, 9700 S. Cass Avenue, Argonne, IL 60439, USA*
[b]*Nuclear Science and Engineering Department, Massachusetts Institute of Technology, 77 Massachusetts Avenue, Cambridge, MA 02139, USA*

ARTICLE INFO

Article history:
Received 21 April 2008
Received in revised form
15 July 2008
Accepted 15 July 2008
Available online 10 October 2008

Keywords:
Steam electrolysis
Stack
Oxygen electrode
Degradation

ABSTRACT

The oxygen electrodes from two solid oxide electrolysis stacks that performed high-temperature steam electrolysis (HTSE) and produced hydrogen for 1000 and 2000 h, respectively, were examined using X-ray fluorescence, X-ray absorption near edge structure (XANES), four-point resistivity, scanning electron microscopy, energy dispersive spectroscopy, X-ray diffraction and Raman micro-spectroscopy to determine possible causes for the degradation in stack performance over the test periods. These techniques yielded information such as elemental distribution, oxidation state, phases present, electrode delamination, and porosity within the electrode layers. From these studies, we found two phenomena that were likely the cause of increasingly poor oxygen electrode performance over time. The first source of degradation was chromium substitution into the oxygen electrode bond layer, which serves to bond the cell to the flow field and interconnect. This is caused by migration of a chromium species from the bipolar plate. The effect of this is a significant increase in the electrical resistance of the bond layer material. The other source of degradation identified was oxygen electrode delamination. The cause of electrode delamination, which is locally catastrophic to the operation of the cell, is unclear; however, we will discuss two possible mechanisms that might cause this phenomenon.

1. Introduction

High-temperature steam electrolysis (HTSE) is a high-efficiency process that generates hydrogen by water-splitting using electricity and heat from an advanced nuclear power plant [1,2]. The process utilizes multiple ceramic cells arranged in ''stacks'', which are identical to solid oxide fuel cell designs, however, for HTSE, the stacks are operated with a reversed current flow and use a mixture of steam and hydrogen as the feed gas. The ''stacking'' of cells provides for a reasonable electrolysis voltage and current, as well as a cell size that is easy to manufacture. However, both increased cell

☆ The submitted manuscript has been created by UChicago Argonne, LLC, Operator of Argonne National Laboratory (''Argonne''). Argonne, a U.S. Department of Energy Office of Science laboratory, is operated under Contract No. DE-AC02-06CH11357. The U.S. Government retains for itself, and others acting on its behalf, a paid-up nonexclusive, irrevocable worldwide license in said article to reproduce, prepare derivative works, distribute copies to the public, and perform publicly and display publicly, by or on behalf of the Government.

* *Corresponding author*. Tel.: +1 630 252 4608; fax: +1 630 972 4452.
E-mail address: mawdsley@anl.gov (J.R. Mawdsley).

0360-3199/$ – see front matter © 2008 International Association for Hydrogen Energy. Published by Elsevier Ltd. All rights reserved.
doi:10.1016/j.ijhydene.2008.07.061

area and a multiplicity of components in the stack introduce many potential sources of defects that can lead to performance degradation over time.

A recent article from Idaho National Laboratory reports the results of a 1000-h test of a Ceramatec, 25-cell planar HTSE stack [2]. This test was conducted under constant applied voltage at 830 °C using a feed gas composition of 54% H_2O, 37% N_2 and 9% H_2. The stack, which had generated hydrogen at a mean rate of 177 NL/h, experienced an overall performance degradation of ~20% over the duration of the test [2]. In 2006, Ceramatec conducted an HTSE demonstration using an integrated laboratory scale (ILS) half-module, which consisted of two stacks of 60 planar solid oxide electrolysis cells, along with the necessary bipolar plates and flow fields assembled in a cross-flow configuration [3]. The test was conducted for 2055 h under constant applied voltage. The temperature of the stack was initially 800–825 °C and had risen to 845–865 °C near the end of the test. The initial feed gas composition was 85% H_2O, 12% H_2 and 3% N_2. After 168 h, CO_2 was fed in with the steam (H_2O:CO_2 = 1:1) to generate syngas ($CO + H_2$) for 1000 h, then the feed gas was returned to the initial composition for the duration of the test. This stack produced 1250 NL/h of hydrogen initially, but experienced an overall performance degradation of ~46% over the duration of the test, most of which occurred in the first 1000 h. This degradation did not appear to be affected by the introduction of or cessation of CO_2 into the feed gas.

After each of these two tests, the stacks were disassembled and a few cells, along with bipolar plates and flow fields, were provided to Argonne for post-test analyses. The objective of this work was to identify the causes of performance degradation within the HTSE stacks. Our approach was to map the surface characteristics of cells and bipolar plates obtained from the disassembled stacks using four-point resistivity measurements and X-ray fluorescence (XRF), followed by closer examination of selected areas using X-ray absorption near edge structure (XANES) measurements, Raman microspectroscopy, X-ray diffraction (XRD), scanning electron microscopy (SEM) and X-ray energy dispersive spectroscopy (EDS). These techniques yielded information such as in-plane resistance, elemental distribution, oxidation state, phases present, electrode delamination and porosity within the electrode layers. In this study, we discuss the results of our investigation of the oxygen electrode compartment of the solid oxide electrolysis (SOEC) cells.

2. Experimental procedures

Cells and bipolar plates were separated from the 25-cell Ceramatec stack [2] and ½ -ILS module [3] for analysis. The electrolyte-supported cells have a 200-μm-thick scandia-stabilized zirconia electrolyte, graded oxygen electrodes consisting of strontium-doped rare earth manganese perovskite oxide mixed with zirconia and (La,Sr)CoO_3 bond layers. The steam/hydrogen electrodes consisted of a nickel-ceria cermet and a nickel bond layer. A schematic representation of a stack repeat unit is shown in Fig. 1. The electrolyte was 10 × 10 cm in dimension, while the electrodes were 8 × 8 cm in dimension, giving a cell active area of 64 cm^2. The bipolar plates were fabricated from ferritic stainless steel. As cells were separated from bipolar plates, separation usually occurred at the bond layers. These layers are applied to either side of the cells and bipolar plates during the stack assembly process to provide good electrical contact. For the 2000-h stack cells, areas where the oxygen electrode and bond layer had delaminated from the zirconia electrolyte could be seen on most of the cells that were sent to Argonne. These areas were primarily along the sealed edge where the steam and hydrogen inlet was located for the steam electrode that was on the other side of the cell. These areas appeared to be the same dark brown color as the electrode material, not white, suggesting that the delamination occurred somewhere within the oxygen electrode near, but not at, the electrode–electrolyte interface. Delaminated areas could not be seen visually on the 1000-h cells.

First, we mapped the resistivity of the exposed surfaces of the cells and bipolar plates using a linear four-point probe (Jandel) to identify possible degraded regions by abnormal increases in resistivity. The outer two contact probes applied a current of 1 mA, while the inner two probes measured the voltage response. The local bulk resistivity, ρ, of the exposed layer of material was calculated using the following equation [4,5].

$$\rho = \frac{4.532Vt}{I} \quad (1)$$

where V is the measured voltage, t is the thickness of the conductive layer and I is the applied current. The four-point probe measures mainly in-plane resistivity with unknown depth information, and the measurements are taken at room temperature. Therefore, the resistivities do not relate directly to the actual resistances during high-temperature stack operation. Nevertheless, regions that have degraded show up as regions of high resistivity compared to the unaffected areas. After testing the as-separated cells, the bond layers were removed with adhesive tape to expose the electrodes and the resistivity mapping procedure was repeated for the 1000-h cells. When we attempted to remove the bond-coat from one of the 2000-h cells, a significant portion of the oxygen electrode layer was peeled away as well. Because of this, we could not make four-point resistivity measurements of the oxygen electrode layer on the 2000-h cells.

To obtain sub-surface information, X-ray fluorescence maps of a 1000-h cell without bond-coat and a 2000-h cell with bond-coat were obtained at Argonne's Advanced Photon Source (APS). The spatial resolution of the maps and images was defined by a scanning step size of 1.5 mm. The X-ray fluorescence spectrum from each position on the sample was collected using a multi-element germanium detector (MED) consisting of 14 probes positioned at various take-off angles ranging from 5° to 35°. The X-ray beam was incident along the z-axis, normal to the sample surface, and the sample was moved in the x-y plane for scanning. The MED was located to the outboard side of the sample with respect to the incident beam. The fluorescence maps were made by analyzing the intensity data from the appropriate energy ranges for each element of interest. Since the MED probes were positioned at different angles with respect to the sample surface, it was possible to obtain a limited depth-dependent profile of elemental distribution. At low take-off angles, the detected

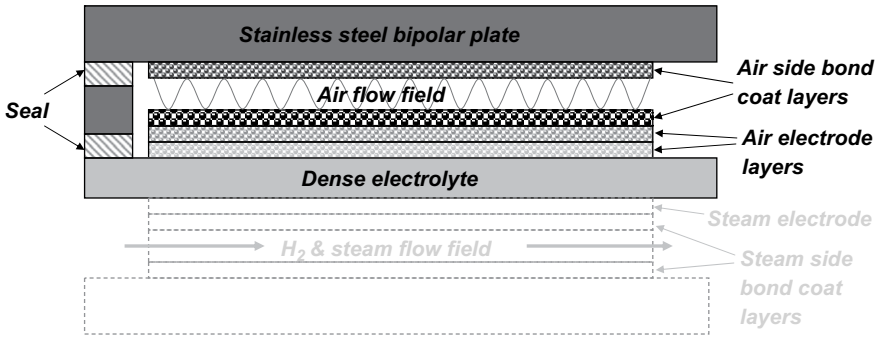

Fig. 1 – Illustration (not to scale) of an HTSE stack repeat unit. The direction of air flow is out of the plane of the page. For clarity, only one set of seals is shown.

X-rays emanate predominantly from nearer the sample surface, whereas X-rays detected at higher take-off angles emanate from locations deeper in the sample. This is due to the strong dependence of the path length on the sine of the take-off angle. To determine the oxidation state of selected elements, XANES measurements were also conducted at five selected points on one of the cells from the 2000-h stack.

From the analyses described above, several regions were identified where performance degradation had likely occurred. We then used SEM, EDS, XRD and Raman micro-spectroscopy to further assess the causes for the degradation in these selected areas. For SEM (JEOL JSM-6400) and EDS (Oxford) analyses, both unpolished plan view samples and polished cross-sections were examined for both the 1000-h and 2000-h cells. XRD (Hitachi) was done on two plan view samples from the 2000-h cell. One XRD pattern was obtained for a piece cut from the area of the cell where the electrode had delaminated and one pattern was obtained from a piece cut from an area where the bond-coat and electrode were still attached to the electrolyte.

Raman micro-spectroscopy was also used to detect known constituent phases and identify unknown impurities within the bond layers and electrodes of a cell from the 1000-h stack. A Renishaw RM2000 Imaging Raman Microscope equipped with a 633 nm HeNe laser excitation source was used for the measurements. Raman spectra were recorded using a 6-μm-diameter laser spot size. The laser power at the sample was 2 mW. This near-surface technique is useful for analyzing features in a non-destructive manner with a variably focused excitation laser. Subsurface phases below the penetration depth of the laser could not be detected without scraping off the surface. Nevertheless, this method was chosen because of the relative ease of identifying known impurities and unexpected phases without having to cut the cells or to coat them with a conductive layer.

3. Results

3.1. *Four-point resistivity probe*

The four-point probe is a simple and fast method to identify areas of degradation by mapping the resistivity of the surfaces. The maps in Fig. 2 illustrate the resistivities of

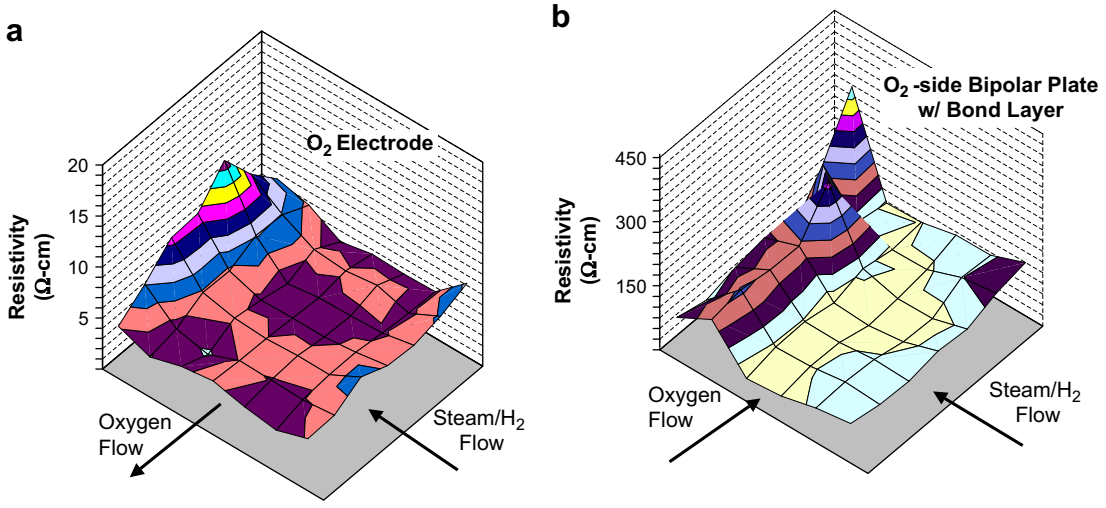

Fig. 2 – Room-temperature, four-point resistivity maps from the 1000-h stack of (a) an oxygen electrode and (b) the O_2-side surface of a bipolar plate with the bond layer. The sealed edges were along the two edges of the cell that are parallel to the oxygen flow.

a 1000-h cell and bipolar plate in the oxygen compartment. Fig. 2(a) shows the results for the oxygen electrode surface after the bond layer was removed. Maps of the bond layer and the electrode for this cell showed similar results. The resistivity is reasonably constant over most of the electrode surface; however, it rises to a maximum along the sealed edge where the hydrogen/steam flow exited the stack (see Fig. 2a).

On the O_2-side of the bipolar plate, mapping of the residual bond layer (Fig. 2(b)) shows a similar ridge of high resistivity along the edge where hydrogen exits the stack. These resistivities are 25 times higher than those of the unaffected regions. The stack performance, however, did not correspond to such high resistances in operation. The reason for this may be that the particles in the bond layer were not as well sintered as were the electrode and bipolar plate surfaces, which made it more difficult to make room temperature four-point resistivity measurements using our apparatus. Nevertheless, the increase in resistivity along the hydrogen exit edge of the stack is clearly evident and it suggests a possible leak in the seal along this edge, affecting both the bond layer and the electrode. This is likely a contributor to the observed long-term degradation [2].

The resistivities measured on the 2000-h cells with bond coat were orders of magnitude higher than those of the 1000-h cells across the whole surface of the cells' active area. The likely cause for this was found when we did our SEM, EDS and XRD analyses, as discussed below.

3.2. *X-ray fluorescence (XRF) mapping*

X-ray fluorescence is a phenomenon that occurs when X-rays are absorbed by atoms. Upon the absorption of an incident X-ray beam, each element emits X-rays with a characteristic set of energies, creating a unique signature for each element [6]. This signature is not dependent on the electronic state of the element, but the intensity of the peaks of the energy signature can indicate the relative concentration of each element. Two types of information were obtained from the X-ray fluorescence experiments. Elemental maps showed the distribution of elements on the surface of the cell with undefined depth information. Rudimentary depth profiles showed the relative abundance of elements as a function of depth into the porous electrode area.

The Mn and Co transition metals are defining elements for the electrode and bond layers, whereas Cr is an impurity that diffuses out of the stainless steel bipolar plate. Fig. 3 shows maps of the distribution of these three elements in an oxygen electrode from the 1000-h stack. Lighter shades of gray indicate a greater elemental abundance. The horizontal lines were tracks left by the flow field channels, which were a corrugated metal, see Fig. 1. The Mn and Co maps (Fig. 3(a and b)) are virtually the negative image of each other on this scale (1 mm), which shows that over the 1000 h of operation, interdiffusion between the two elements was limited. The large patch in the upper left corner is a residue of the bond layer that had sintered to the electrode and could not be removed.

Chromium had deposited in all areas of the active electrode, particularly along the edges near the gas seals, as shown in Fig. 3(c). In these areas, excess Cr is a result of the bipolar plate edge rail being in proximity to the electrode. These areas also correspond to the areas of high resistivity in Fig. 2(a). However, chromium did not deposit on the exposed zirconia edges of the cell. This demonstrates that Cr deposition is confined to the electrically active region in the electrode. Additionally, the Cr transport appears to be affected somewhat by carrier gas flow, as flow patterns can be seen that are related to the flow of air through the cell. Chromium has been shown to poison the oxygen reduction reaction in solid oxide fuel cells [7], and it is suspected that the same phenomenon causes degradation in steam electrolysis cells as well. This is of particular concern when Cr deposits at the electrode–electrolyte interface where the oxygen reaction occurs. Depth information was needed to determine if, in the cell being examined, Cr had deposited at the electrode–electrolyte interface.

The depth profile illustrated in Fig. 4 was constructed using the Mn or Cr ratio of data obtained from two detectors positioned at high and low take-off angles. The zirconia at the cell's edges has been masked to cover the background noise associated with taking the ratios of small numbers. In this figure, the darker gray indicates that Mn or Cr is near the surface and lighter shades indicate that the element has diffused deeper into the electrode. The patch in the upper left corner of Fig. 4(a) shows that the electrode is buried under the bond layer, whereas Cr (Fig. 4(b)) lies near the surface. In the exposed electrode region, Mn is at the surface and, in comparison, Cr has migrated deeper towards the electrolyte interface. The high relative abundance of Cr near the electrolyte interface may have contributed to stack degradation.

The Cr XRF map of an oxygen electrode with bond coat layer from the 2000-h stack is shown in Fig. 5. The inactive edges of the cell and areas where the electrode had delaminated did not contain appreciable Cr and appear dark. The lighter areas show that there was significant Cr in the bond layer of the 2000-h cell. As compared to the 1000-h cell (Fig. 3(c)), the Cr found in the 2000-h cell does not appear to be concentrated near the sealed edges. This is likely due to the fact that the stainless steel edge rails were placed further from the electrodes in the 2000-h stack.

3.3. *X-ray absorption near edge structure (XANES)*

XANES is an element-specific technique in which an increase in absorption of the incident beam is observed when the energy of that beam is equal to the binding energy of a core-level electron. Chemical information such as valence and coordination environment can be derived from XANES spectra. For a detailed explanation of XANES, please see Ref. [8]. XANES was used to determine the oxidation state of the Cr because it is the only nondestructive method available for the type of samples that we have [9]. To determine the oxidation state of the chromium found in the oxygen side bond coat layer of the 2000-h cell using XRF mapping, XANES measurements were conducted in five different locations, which are marked as A–E in Fig. 5, on the 2000-h cell in regions where the bond-coat was still attached. The results of all five XANES measurements are shown in Fig. 6. The primary finding from these measurements is the presence of hexavalent chromium in all five areas measured. The pre-edge peak at 5994 eV indicates the presence of Cr^{6+} in the bond layer [10,11]. The

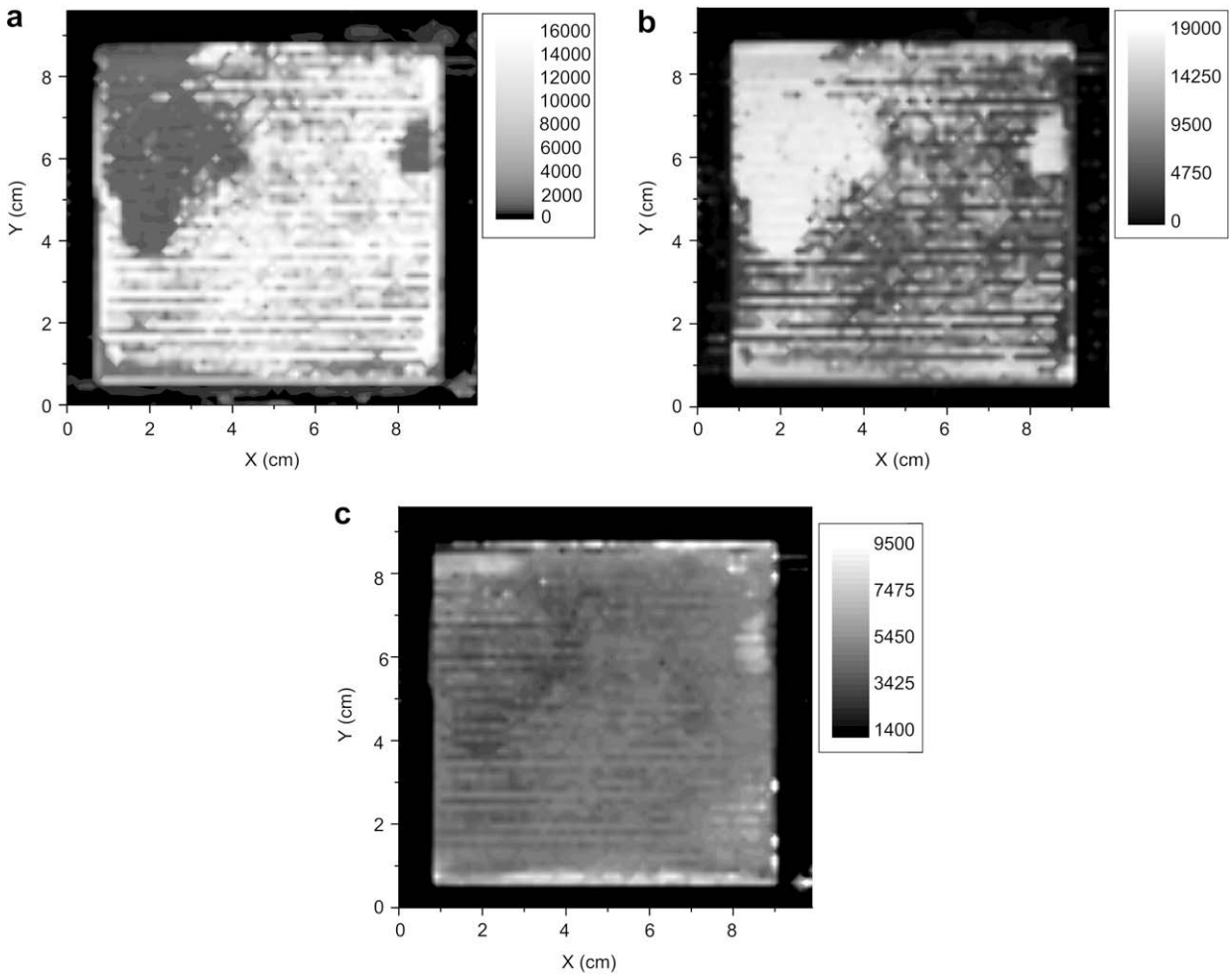

Fig. 3 – X-ray fluorescence maps of (a) Mn, (b) Co and (c) Cr abundance in the oxygen electrode of a 1000-h cell. Lighter shading corresponds to a greater concentration of the element. The direction of the oxygen flow over the cell was from right to left. The sealed edges were along the top and bottom edges of the cell.

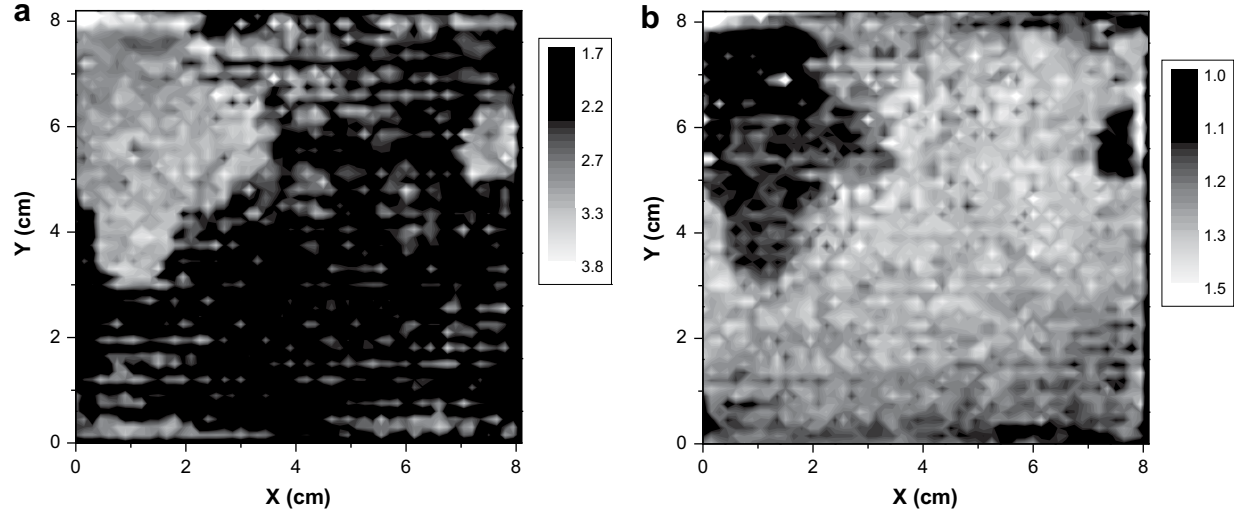

Fig. 4 – Depth profile of (a) Mn and (b) Cr in the 1000-h oxygen electrode. Darker shading corresponds to more of the element near the surface and lighter shading corresponds to greater buried element abundance. Oxygen flowed over the electrode from right to left. The zirconia edges have been masked.

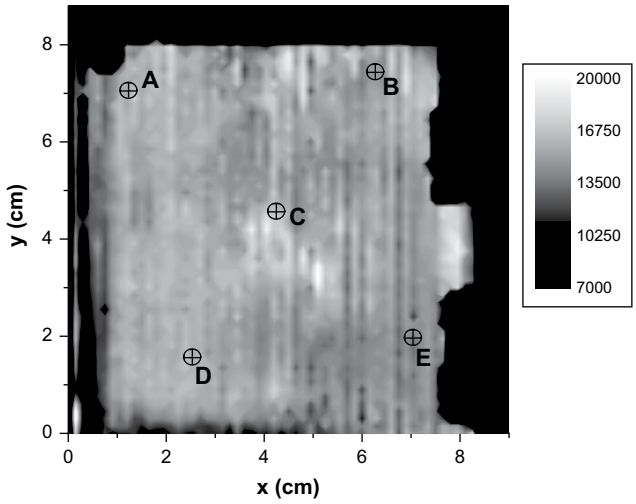

Fig. 5 – X-ray fluorescence map of Cr for a 2000-h cell oxygen electrode with bond-coat layer. The edges of the cell were masked on the bottom and left side of the image. Lighter areas correspond to the highest concentration of Cr and the black area indicates no Cr present. The markers A–E indicate the five positions where XANES measurements were made on this sample. The oxygen flowed from bottom to top during stack operation.

order of Cr^{6+} abundance found for the five areas measured (see Fig. 4) is C > B > A > E>D. The results indicate that the highest concentration of Cr^{6+} is near the center of the electrode, area C. It is noteworthy that Cr^{6+} is a very volatile form of Cr at 800 °C [12–15].

3.4. *Scanning electron microscopy (SEM) and X-ray energy dispersive spectroscopy (EDS)*

Selected pieces of both the 1000-h and the 2000-h cells were examined by SEM in plan view and cross-section. One sample

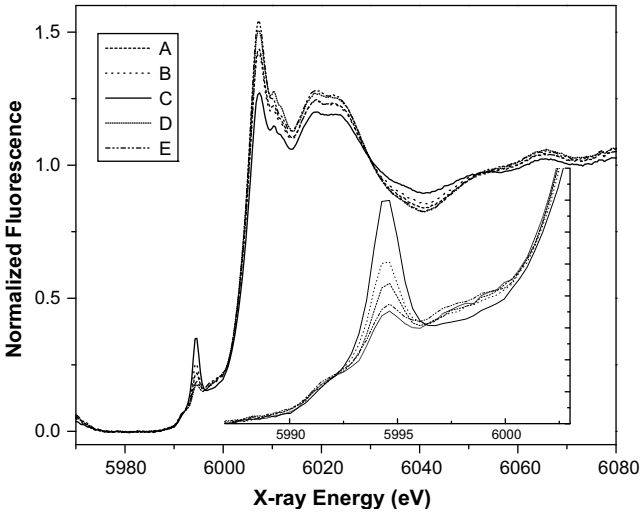

Fig. 6 – Cr XANES spectra for the five locations shown in Fig. 5, on the oxygen electrode of a 2000-h cell. The pre-edge peak at 5995 eV indicates the presence of Cr^{6+} in the bond layer.

was a plan view of the oxygen side of the 2000-h cell that contained a delaminated region and a region of the air electrode and bond layer still intact. It was taken from the steam-in, oxygen-out corner of the cell. An SEM image of the delaminated region is shown in Fig. 7. The dark area in the center of the image is bare electrolyte, whereas the lighter areas are where a very thin layer of the electrode remains. EDS results taken from the dark central region labeled area 1 reveals only the elements in the electrolyte. The EDS results taken from the region labeled area 2 show all of the elements in the electrolyte and in the oxygen electrode. Most of the delaminated areas viewed by SEM resembled area 2, with grains from the electrode material still visible, which explains why the delaminated areas looked dark brown (cathode) and not white (electrolyte). An SEM image of the region that still had the electrode and bond layer attached is shown in Fig. 8. Looking down on the electrode in the plan view, the top layer is the bond-coat layer of Sr-doped $LaCoO_3$. In Fig. 8, this appears as fine-grained material with cracks in it. The large grains on top of the bond layer were unexpected. These were found to contain primarily Cr, Co, and O by EDS, with a Cr to Co ratio of approximately 9:7. Grains containing primarily Cr, Co, and O were also found on the bond-coat top surface of the 1000-h cell. In this case, the grains were much smaller, about 1-3 μm in diameter and the Cr:Co ratio was 2:3.

Using the data from the X-ray fluorescence measurements, 2-cm-long sections were cut out of both the 1000-h and 2000-h cells near the edge of the electrode. Fig. 9 shows SEM images of one of the 2000-h cell cross-sections, which was cut from the steam-in, oxygen-out corner of the cell. Fig. 9(a) shows that the electrode had delaminated even though this area appeared to have been attached when initially inspected. This was also seen in the cross-section of the oxygen-in, hydrogen-out corner of the cell, which did not appear visibly delaminated. Only one small oxygen electrode delamination was found in the cross-sections of the 1000-h cell examined. Fig. 9(b) shows a high magnification image of the bond-coat and oxygen electrode in an area of the sample where both were attached to the electrolyte. EDS data were taken

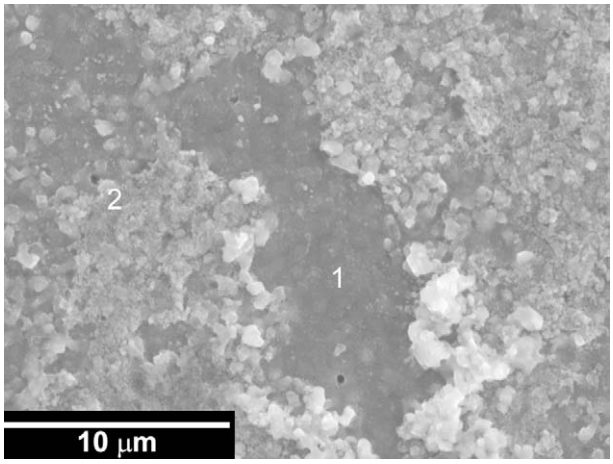

Fig. 7 – SEM plan view micrograph of a delaminated area on the oxygen side of a 2000-h cell. Area 1 – bare electrolyte. Area 2 – electrolyte + oxygen electrode.

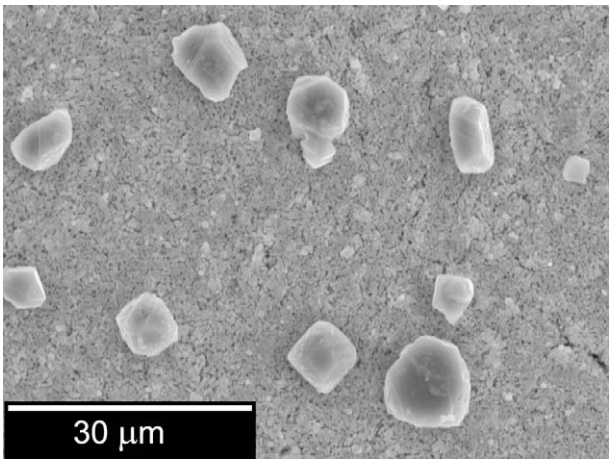

Fig. 8 – SEM micrograph of the plan view (top surface) of the bond-coat layer of the oxygen electrode from a 2000-h cell. The large particles on top of the bond layer surface are a reaction product phase that formed during operation of the stack.

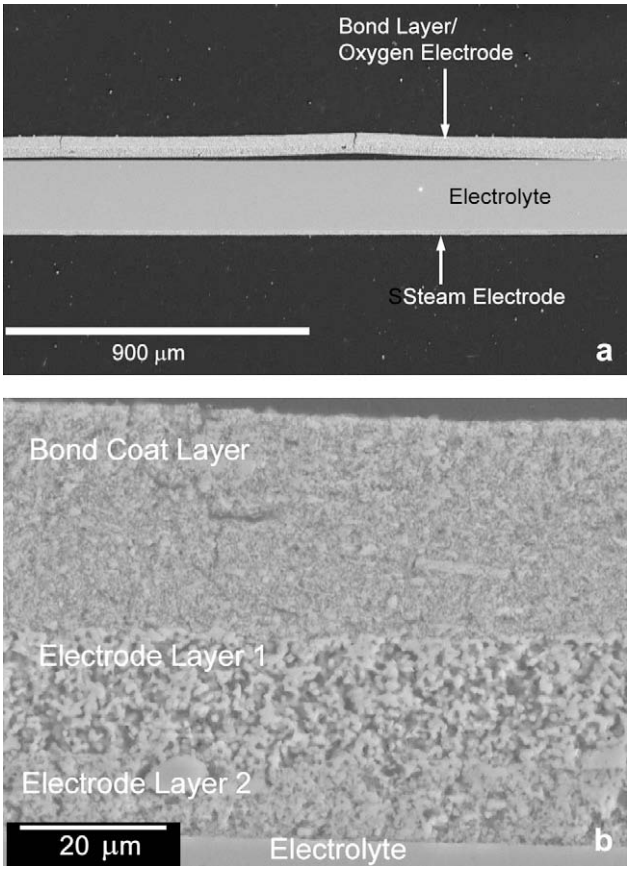

Fig. 9 – SEM micrographs of a polished cross-section of a cell from the 2000-h stack (near the oxygen exit, steam inlet corner): (a) area where the oxygen electrode delaminated, (b) area where the bond-coat and oxygen electrode are still attached to the electrolyte.

throughout the bond-coat layer and both electrode layers. For the 2000-h cell there was as much as 10 at.% Cr at the upper boundary of the bond-coat. At the lower boundary of the bond-coat (approximately half way down in the SEM image of Fig. 9(b)), we observed only about 3 at.% Cr. Using EDS to determine Cr content in the oxygen electrode layers becomes difficult because the lines for the elements in the oxygen electrode overlap with the Cr lines. Nonetheless, we estimated that there was less than 1% Cr in the oxygen electrode based on the analysis models provided by the EDS software (INCA). It appears that the (La,Sr)CoO_3 did absorb most of the Cr migrating from the bipolar plates and flow fields in the 2000-h cells. This pattern of Cr contamination was found in every location that we examined. In the 1000-h cell, the concentration of Cr at the free surface of the bond layer was 3–4 at.%, indicating that the amount of Cr contamination increased over time.

3.5. *X-ray diffraction*

Glancing angle X-ray diffraction measurements on a piece of the 2000-h cell, with the bond-coat entirely intact, taken from the air inlet side of the cell revealed a spinel phase, $(AB)_3O_4$, which is the expected crystal structure of a Cr–Co–O compound. This pattern is shown in Fig. 10(a). No evidence of a free lanthanum oxide or strontium oxide phase was observed in any of the patterns. X-ray diffraction of a delaminated area from the air inlet side of the cell (Fig. 10(b)) revealed a peak that corresponds to $SrZrO_3$, which is an undesirable reaction product that can be formed between the Sr-containing electrode material and the electrolyte. This phase is an insulating phase that has also been observed to form in solid oxide fuel cell materials studies [16]. However, because the relative intensity of the $SrZrO_3$ peak is small and was only found in this one location, it is unlikely that the formation of this phase made a large contribution to the stack performance degradation that was observed.

3.6. *Raman micro-spectroscopy*

The exposed surface of a cell from the 1000-h stack was examined by Raman micro-spectroscopy to identify any reaction phases that may have been formed during stack operation. Raman spectra of the electrode matrix (Fig. 11(d)) showed the prominent presence of cubic ZrO_2 and a perovskite phase. Areas of tetragonal and monoclinic ZrO_2 were also identified, but were mostly located around the edges of the electrolyte plates, as shown in Fig. 11(a and b). The transition from tetragonal to monoclinic ZrO_2 can either be beneficial through a toughening mechanism, or it can be damaging, leading to cracking, depending on the volume fractions and grain sizes of the cubic, tetragonal and monoclinic phases [17]. The spectrum of a cobalt-containing spinel phase (Fig. 11(c)) was observed in a few locations on the surface of the bond-coat of the 1000-h cell.

4. Discussion

From the results presented above, we concluded that there are two primary degradation phenomena affecting the oxygen

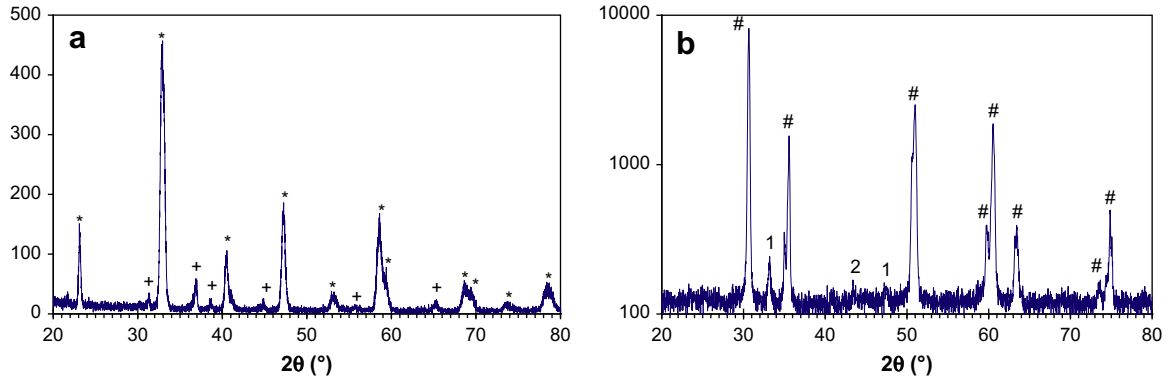

Fig. 10 – X-ray diffraction patterns from different regions of the oxygen side of the 2000-h cell: (a) top surface of the bond-coat, * = (La,Sr)CoO_3, + = Co_2CrO_4, (b) delaminated area at the steam inlet edge, # = zirconia electrolyte, 1 = electrode material, 2 = $SrZrO_3$.

electrodes in high-temperature steam electrolysis stacks. The first is the chromium contamination of the bond-coat layer and, to a lesser extent, the oxygen electrode layers beneath. The second and more damaging phenomenon is delamination of the oxygen electrode. The proposed mechanisms by which these two phenomena occur and their implications on stack performance are discussed below.

Cr is a known poison for SOFC oxygen electrodes [12], and we suspect that the amounts that we have detected in the bond layer using EDS, i.e., up to 10 at.%, contributed to the stack performance degradation. The evidence of Cr^{6+} seen in the XANES spectra shown in Fig. 6 indicates that Cr is transported from the stainless steel separator plate via a vapor phase, such as CrO_3 or $CrO_2(OH)_2$, to the bond-coat surfaces below. This has also been reported to occur in the solid oxide fuel cell literature [12]. Thermodynamic data show that the relative magnitudes of the Gibbs free energies of formation (ΔG_f°) of compounds similar to those in our materials system at 800 °C are as follows: $LaCrO_3$ (−1250 kJ/mol [18]) < $LaMnO_3$ (−1149 kJ/mol [19]) < $CoCr_2O_4$ (−1056 kJ/mol [20]) < $LaCoO_3$ (−942 kJ/mol [21,22]). This makes $LaCrO_3$ and $CoCr_2O_4$ more thermodynamically stable than $LaCoO_3$. The EDS data combined with the XRD and Raman results indicate the following scenario. No non-perovskite strontium or lanthanum containing phases were observed either by XRD or Raman. Therefore, we conclude that the cobalt must have been liberated from the bond-coat of (La,Sr)CoO_3 to form the $(Cr,Co)_3O_4$ spinel. Co must have been replaced in the (La,Sr)-CoO_3 structure by Cr because the perovskite crystal structure is not very stable with vacancies on the B-sites [23]. While the $(Cr,Co)_3O_4$ crystals shown in Fig. 8 would not be expected to affect the performance of the stack, the level of substitution of Cr for Co on the B-site in the perovskite bond-coat could be as much as 50% of the B-site atoms, based on the EDS data. This could lead to an increase in the resistance of the bond-coat by as much as an order of magnitude at 800 °C [24,25]. An increase in resistance of this magnitude is consistent with our four-point resistivity measurements at room temperature.

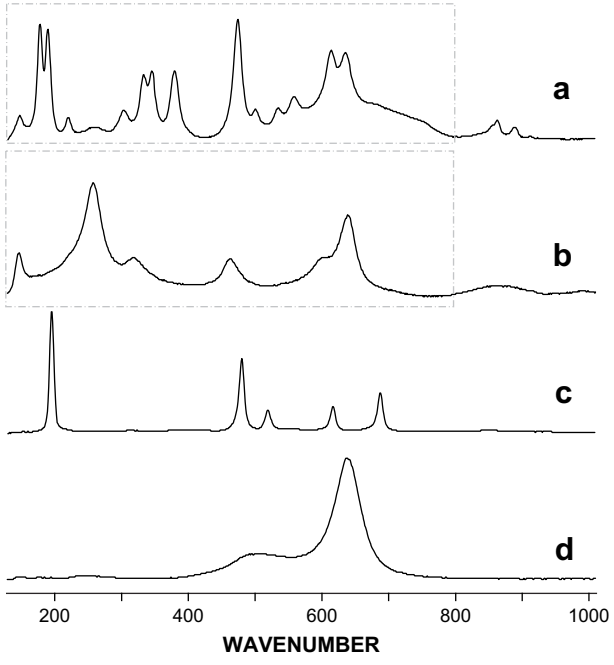

Fig. 11 – Raman spectra of the oxygen electrode side of the 1000-h cell: (a) monoclinic ZrO_2 spectra observed on the bare electrolyte at the edge of the cell, (b) tetragonal ZrO_2 observed on the bare electrolyte at the edge of the cell, (c) characteristic five-peak cobalt-spinel spectrum observed at various places on the surface of the bond-coat and (d) spectra of the matrix of the electrode layer showing a perovskite peak at 500 cm^{-1} and a cubic ZrO_2 peak at 640 cm^{-1}.

As mentioned above, on most of the 2000-h cells, we found areas where the oxygen electrode delamination appeared to have occurred prior to separating the cells from the stack. The largest delaminated areas were found at the sealed edge where the steam inlet was located. This is the edge of the oxygen electrode that experiences the highest current density and, thus, the highest amount of oxygen evolution. It was also noted above that we were able to easily remove a significant portion of the oxygen electrode layers on one of the 2000-h cells with cellophane tape even though, after 2000 h, the electrodes should have been well bonded. The ease with which we were able to peel away these layers, and the SEM

micrograph in Fig. 7 of an area that was apparently delaminated during stack operation, indicates some defect(s) at or near the oxygen electrode–electrolyte interface. There has been only one other report of oxygen electrode delamination during high-temperature steam electrolysis [26]. Oxygen electrode delamination when solid oxide fuel cells have been operated in electrolysis mode has been reported in a few instances [27–29], and electrode delamination has also been reported in a proton exchange membrane (PEM) fuel cell that was operated as a water electrolyzer [30]. We offer two possible reasons for the observed delamination of the oxygen electrode. First, a restriction in the ability of the oxygen to diffuse into the flow field above the electrode due to over-sintering of the electrode or bond layer could cause enough pressure build up to cleave the oxygen electrode grains and cause delamination. Our SEM investigation does show some possibility for over-sintering in the Electrode 1 layer, as seen in Fig. 9(b), but it is difficult to determine if the flow was constricted enough to cause a pressure build-up large enough to cleave the electrode. Second, high oxygen flux at the electrode–electrolyte interface may lead to a mismatch between the greater ability of zirconia to release oxygen and the lesser ability of the electrode material to conduct oxide ions away. If this is the case, then any defect at the solid–solid interface between the two materials could serve as a nucleation point where oxygen could be released after the electron is transferred to the electrode. Under continuous operation, more oxygen would be released into this defect, pressure would build up, and the defect would grow into a crack that would eventually cleave the perovskite–zirconia interface(s). Since the electrode material in our cells was a mixture of zirconia and perovskite, this might explain why the delamination occurred more often within the electrode, but close to the electrolyte interface, as seen in Fig. 7. At present, we can neither prove that this phenomenon was occurring in our cells nor eliminate this possibility, however, evidence for this delamination mechanism was shown by Brichzin et al. [29]. They found that bubbles formed at the electrode–electrolyte interfaces of their dense film samples under high anodic polarization. Further investigation is needed to verify the cause of the oxygen electrode delamination, whether it is a pressure build-up within the electrode layer due to over-sintering, defects acting as nucleation sites for localized cracking of the perovskite–zirconia interfaces within the electrode layer, or a combination of the two phenomena.

5. Conclusions

Two high-temperature steam electrolysis stacks that had operated for over 1000 and 2000 h, respectively, at ~830 °C were disassembled and the oxygen electrodes in some of the cells were examined to identify potential causes of stack performance degradation over the test periods. Using the composition and conductivity mapping approaches with XRF and four-point resistivity measurements, we were able to identify regions of interest where performance degradation most likely occurred. We then used XANES, SEM, EDS, XRD and Raman micro-spectroscopy to further analyze those regions. Our results revealed two primary causes of stack degradation: (1) Cr substitution for Co in the (La,Sr)CoO_3 bond-coat layer that significantly lowered the electrical conductivity of the bond-coat and (2) partial oxygen electrode delamination. XANES measurements indicated that a vapor phase containing Cr^{6+} had diffused from the ferritic stainless steel bipolar plate towards the electrode–electrolyte interface. SEM, EDS, XRD and Raman micro-spectroscopy identified a cobalt and chromium containing spinel phase on the surface of the bond-coat layers. EDS, XRD and Raman results indicated that as much as 50% of the Co in the perovskite lattice of the bond-coat had been replaced by Cr. Areas of oxygen electrode delamination were observed visually, particularly on the steam inlet side of the cell. SEM of cell cross-sections revealed that delamination was also present in areas that had appeared to be intact. Electrode delamination is catastrophic and is probably the largest contributor to stack performance degradation. The exact reason for the delamination is not clear, but a high rate of oxygen release into any defect at the perovskite–zirconia interfaces within the electrode layer may have caused localized pressure-induced cracking of the interfaces. There is also the possibility that over-sintering of the electrode layer lead to the formation of closed porosity that blocked the flow of oxygen away from the triple-phase boundaries, which caused a pressure build-up in the electrode layer that caused the observed delamination. More study is needed to characterize and prevent this phenomenon from occurring in HTSE stacks.

Acknowledgements

The authors are grateful to Deborah Myers, Mark Petri, Theodore Krause, Terry Cruse, John Vaughey, Ann Call, Magali Ferrandon and Nathan Styx of Argonne National Laboratory for their valuable assistance and input. Thanks to Joseph Hartvigsen, S. Elangovan and Dennis Larsen of Ceramatec, Inc. for supplying the stack components for this study and for their useful input. Thanks to Steven Herring, Carl Stoots, Jim O'Brien and Grant Hawkes of Idaho National Laboratory for their support and helpful discussions. This research was funded by the Nuclear Hydrogen Initiative of the U.S. Department of Energy, Office of Nuclear Energy, Science and Technology. Argonne National Laboratory is operated for the U.S. Department of Energy by UChicago Argonne, LLC, under contract DE-AC02-06CH11357. Use of the Advanced Photon Source was supported by the U. S. Department of Energy, Office of Science, Office of Basic Energy Sciences. Materials Research Collaborative Access Team (MRCAT) beamline operations at the APS were supported by the Department of Energy and the MRCAT member institutions. Scanning electron microscopy and EDX were carried out at the Analytical Chemistry Laboratory at Argonne National Laboratory.

REFERENCES

[1] Doenitz W, Schmidberger R, Steinheil E, Streicher R. Hydrogen production by high temperature electrolysis of water vapor. Int J Hydrogen Energy 1980;5(1):55–63.

[2] O'Brien JE, Stoots CM, Herring JS, Hartvigsen JJ. Performance of planar high-temperature electrolysis stacks for hydrogen

production from nuclear energy. Nucl Technol 2007;158(2): 118–31.
[3] Hartvigsen JJ, Elangovan S, Nickens A. Test of high temperature electrolysis ILS half module. In: U.S. DOE Hydrogen Program FY 2007 Annual Progress Report; 2007. p. 234–37.
[4] Logan MA. Sheet resistivity measurements on rectangular surfaces-general solution for four point probe conversion factors. Bell Syst Tech J (USA) 1967;46(10):2277–322.
[5] Smits FM. Measurement of sheet resistivities with the four-point probe. Bell Syst Tech J (USA) 1958;37(3):711–8.
[6] Jenkins R, Gould RW, Gedcke D. Quantitative X-ray spectrometry. New York: Marcel Dekker; 1981.
[7] Ingram BJ, Cruse TA, Krumpelt M. Potassium-assisted chromium transport in solid oxide fuel cells. J Electrochem Soc 2007;154(11):B1200–5.
[8] Bianconi A. X-ray absorption: principles, applications, techniques of EXAFS, SEXAFS, and XANES. In: Koningsberger DC, Prins R, editors. Chemical Analysis92. New York: Wiley; 1988.
[9] Bajt S, Clark SB, Sutton SR, Rivers ML, Smith JV. Synchrotron X-ray microprobe determination of chromate content using X-ray-absorption near-edge structure. Anal Chem 1993; 65(13):1800–4.
[10] Peterson ML, Brown GE, Parks GA, Stein CL. Differential redox and sorption of Cr(III/VI) on natural silicate and oxide minerals: EXAFS and XANES results. Geochim Cosmochim Acta 1997;61(16):3399–412.
[11] Arcon I, Mirtic B, Kodre A. Determination of valence states of chromium in calcium chromates by using X-ray absorption near-edge structure (XANES) spectroscopy. J Am Ceram Soc 1998;81:222–4.
[12] Fergus JW. Effect of cathode and electrolyte transport properties on chromium poisoning in solid oxide fuel cells. Int J Hydrogen Energy 2007;32:3664–71.
[13] Ebbinghaus BB. Thermodynamics of gas-phase chromium species—the chromium oxides, the chromium oxyhydroxides, and volatility calculations in waste incineration processes. Combust Flame 1993;93(1–2):119–37.
[14] Gindorf C, Singheiser L, Hilpert K. Chromium vaporisation from Fe, Cr base alloys used as interconnect in fuel cells. Steel Res 2001;72(11,12):528–33.
[15] Gindorf C, Singheiser L, Hilpert K. Vaporisation of chromia in humid air. J Phys Chem Solids 2005;66:384–7.
[16] Ralph JM, Rossignol C, Kumar R. Cathode materials for reduced-temperature SOFCs. J Electrochem Soc 2003;150(11): A1518–22.
[17] Stevens R. An introduction to zirconia: zirconia and zirconia ceramics. 2nd ed. Twickenham, UK: Magnesium Electron Ltd.; 1986.
[18] Scientific Group Thermodata Europe. In: Theoretische Hüttenkunde Lehrstuhl für, Aachen Rheinisch-Westfälische Technische Hochschule, editors. Thermodynamic properties of inorganic materials, subvolume A: pure substances. Part 3: compounds from $CoCl_3$ to Ge_3N_4. Landolt–Börnstein – Group IV physical chemistry, vol. 19. Berlin: Springer-Verlag; 2000.
[19] Scientific Group Thermodata Europe. In: Theoretische Hüttenkunde Lehrstuhl für, Aachen Rheinisch-Westfälische Technische Hochschule, editors. Thermodynamic properties of inorganic materials, subvolume A: pure substances. Part 4: compounds from HgH to ZnTe. Landolt–Börnstein – Group IV physical chemistry, vol. 19. Berlin: Springer-Verlag; 2001.
[20] Barin I. Thermochemical data of pure substances. Part I: Ag–Kr. 2nd ed. Weinheim, Germany: VCH; 1993.
[21] Parida SC, Singh Z, Dash S, Prasad R, Venugopal V. Standard molar Gibbs energies of formation of the ternary compounds in the La–Co–O system using solid oxide galvanic cell method. J Alloys Compd 1999;285:7–11.
[22] Cheng J, Navrotsky A, Zhou X, Anderson HU. Enthalpies of formation of $LaMO_3$ perovskites (M = Cr, Fe, Co, and Ni). J Mater Res 2005;20(1):191–200.
[23] Peña MA, Fierro JLG. Chemical structures and performance of perovskite oxides. Chem Rev 2001;101(7):1981–2017.
[24] Tsvetkov DS, Zuev AY, Vylkov AI, Petrov AN. Oxide ion transport in undoped and Cr-doped $LaCoO_{3-\delta}$. Solid State Ionics 2007;178:1458–62.
[25] Kharton VV, Yaremchenko AA, Naumovich EN. Research on the electrochemistry of oxygen ion conductors in the former Soviet Union. II. Perovskite-related oxides. J Solid State Electrochem 1999;3:303–26.
[26] Guan J, Minh N, Ramamurthi B, Ruud J, Hong J, Riley P, Weng D. High performance flexible reversible solid oxide fuel cell, Final Technical Report to the U.S. Department of Energy; 2007.
[27] Virkar AV, Nachlas J, Joshi AV, Diamond J. Internal precipitation of molecular oxygen and electromechanical failure of zirconia solid electrolytes. J Am Ceram Soc 1990; 73(11):3382–90.
[28] Kaiser A, Monreal E, Stolten D. Preparation techniques and materials for long term stable sofc—single cell membranes. Ionics 1997;3:143–8.
[29] Brichzin V, Fleig J, Habermeier H-U, Cristiani G, Maier J. The geometry dependence of the polarization resistance of Sr-doped $LaMnO_3$ microelectrodes on yttria-stabilized zirconia. Solid State Ionics 2002;152-153:499–507.
[30] Song S, Zhang H, Liu B, Zhao P, Zhang Y, Yi B. An improved catalyst-coated membrane structure for PEM water electrolyzer. Electrochem Solid State Lett 2007;10(8): B122–5.